Received: 7 August 2020 | Revised: 3 February 2021 | Accepted: 19 February 2021

IET Microwaves, Antennas & Propagation

DOI: 10.1049/mia2.12116

The Institution of Engineering and Technology WILEY

ORIGINAL RESEARCH PAPER

Characterization of a 60 GHz scattered wireless channel with different antenna polarizations for underground multimedia applications

Shah Ahsanuzzaman Md Tariq[1] | **Charles L. Despins**[2] | **Sofiène Affes**[3] | **Chahé Nerguizian**[1]

[1]Electrical Engineering, Université de Montréal-École Polytechnique, Montreal, Quebec, Canada

[2]Electrical Engineering, Université du Québec-École de technologie supérieure, Montreal, Quebec, Canada

[3]Electrical Engineering, Université du Québec-INRS-EMT, Montreal, Quebec, Canada

Correspondence

Shah Ahsanuzzaman Md Tariq, Electrical Engineering, Université de Montréal-École Polytechnique, Montreal, Canada.
Email: tariq.shah-ahsanuzzaman-md@polymtl.ca

Funding information

Natural Sciences and Engineering Research Council of Canada, Grant/Award Number: RDCPJ 460985 - 13

Abstract

Large scale (i.e. <10 m) and small scale (i.e. 1 × 1× 1 cm) measurements and characterization of a scattered wireless channel with different antenna polarizations and configurations in the underground mine galleries at 60 GHz are addressed. Results show that the rough surface scattering and the gallery dimensions affect the path loss (PL) exponent and it becomes smaller than the free space. Vertically polarized antennas give a lower value of the PL exponent and root mean square (RMS) delay spread compared to the horizontal one. The small scale 3D measurement results show that the power loss of around 1–5 dB within a small scale cubical area. Results also show that the channel is less time dispersive in a wider gallery and observed a higher value of the RMS delay spread compared to a smaller gallery. The statistical results of the small scale multipath amplitude fading provide a better fit with the Rician distribution. The effects such as scattering, polarization, antenna radiation patterns, and waveguide which caused increase and decrease of the value of PL exponent and delay spread are also analysed. Results revealed that a directional narrow beam dual-polarized antenna configuration might be a good candidate in this environment.

1 | INTRODUCTION

Nowadays, short-range wireless communications offer huge possibilities to provide seamless multimedia services. Recently, the 60 GHz band has generated significant interest because of its high data rate (i.e. >1 Gbps) capability within a short-range communication in indoor environments [1]. However, the utility of wireless communications is also essential for safety and productivity particularly in an underground mine environment [2, 3]. Besides the multimedia services (voice, video, and data), wireless communications are used for geo-localization of miners and equipment, speedy rescue operation of trapped miners under debris etc. In the mining industry, the well-known Through The Earth communication systems are used for vehicle tracking, monitoring, and controlling. Other systems such as radio-frequency identification, Zigbee, wireless sensor networks, and Wi-Fi systems are also convenient to use in underground mine. The use of the Internet of Things and aerial drones could be a solution for a faster wireless safety system. Those solutions could be implemented at the lower frequency bands such as 2.4, 5.8 GHz, however, those systems may not be enough to provide a high quality of multimedia services to a dense network in a larger mine gallery length due to the lower bandwidth and higher interference. Triband (2.4, 5.8, and 60 GHz) solution, however, could provide a wireless solution to fulfil the mining industry requirements [4, 5]. The industry requirements such as the optimum attenuation, lower interference, low latency, and high accuracy of geolocalization in a dense wireless network are highlighted herein to design a wireless system for the underground mining environment.

The 60 GHz band, which has an oxygen absorption feature in the propagation phenomenon and additional features such as low interference, unlicensed spectrum, larger bandwidth, smaller package size, and beamforming capability can possibly fulfil many of the mining industry's technical requirements. Therefore, the 60 GHz bands could be used for the small cell

backhaul point to point link for the applications of video monitoring, remote control of vehicles, three-dimensional (3D) mapping, and creating virtual environments, cooperative robotic systems for remote operation of mineral extraction etc. However, the 60 GHz bands may suffer from dispersion, absorption, scattering on the wireless channel because of short wavelength, and the complex structure of the mine surface.

For more than a decade, several measurement campaigns were carried out for the wireless channel characterization in an experimental mine called Canada Centre for Mineral and Energy Technology (CANMET), by the Laboratoire deRecherche Télébec en Communications Souterraines (LRTCS), located in Val-d'Or, QC, Canada. Some of the experimental results are listed in Table 1. Comparative results show that as the operating frequency increases and the antenna half-power beamwidth (HPBW) decreases, a lower value of RMS delay spread is obtained. The values of the path loss (PL) exponent are found to be around 2. The results revealed that the PL exponent and the delay spread particularly depend on the antenna HPBW, topology of the experiment, gallery curvature, and operating wavelength as well as the transmitter receiver separation distance (Tx-Rx). Measurements with a heavy vehicle between inside and outside of the CANMET mine gallery have also been carried out in a frequency range between 2 and 6 GHz [17]. The results showed that the PL exponent is found to be approximately 2.23 and 1.96 when a scoop vehicle was inside and outside of the gallery, respectively. The average values of RMS delay spread of the inside and outside gallery were also found to be around 5.02 and 3.85 ns, respectively.

Other measurements carried out in different mines and tunnels in different frequencies are reported in [18–21]. Emslie et al. [19] performed a measurement in a coal mine at 200–4000 MHz and noted that the increase of a signal power loss is caused by the surface roughness and the tilt of the tunnel walls. At 900 MHz and 1.8 GHz, Zhang et al. [20] reported that the RMS delay spread is less than 25 ns for a straight empty subway tunnel and increased to 103 ns when vehicles were presented.

However, measurements carried out at 60 GHz bands in indoor environments are reported in [22–28]. Smulders et al. [22, 23] reported a PL exponent of less than 2 with the signal fading between 0.14 dB and 2.14 dB and an RMS delay spread of 1 ns with a fan-pen antenna configuration. Channel fading and dispersion effects in an indoor environment were also well studied by Geng [24], where the obtained PL exponent was found to be less than the free space value due to the waveguide effect.

As well, 60 GHz measurement results with different antenna polarizations showed that the use of a circular polarization of an antenna can outperform than the use of a linear polarization in terms of bit error rate in the library, hallway, and residential environments [25]. Results also showed that the number of strong reflected waves depends on the types of polarization such as horizontal and vertical [26]. Moreover, polarization diversity and dual polarization transmission systems may suffer from the antenna polarization mismatch. The angle of arrivals (AoAs) of the strong reflected waves may also depend on the polarization types due to the variation in the value of reflection coefficients [26]. Manabe et al. [27] found that the RMS delay spread value with horizontal (H) polarization is slightly lower than with vertical (V) polarization. Zhao et al. [28] noted that the vertical polarization of a 60 GHz transceiver resulted in a higher received power than with the horizontal polarization in the shadowing region. The IEEE 802.15.3c task group also demonstrated that the mismatch of polarization characteristics between transmitting and receiving antennas at 60 GHz could result in 10–20 dB received power degradation [29].

In the analysis of the polarization effect in underground mines and tunnels, Cawley et al. [30] found that different polarizations have different coupling losses, attenuations, and bend losses. Zhang et al. [31] also described the received power losses with different polarization types at 900 MHz. Bashir et al. [32] also found that the PL is more sensitive to antenna position and polarization than the time dispersion in underground mines and tunnels over 2.4–4 GHz. In contrast, the antenna polarizations have a significant impact on the channel characterizations at lower frequency bands. Therefore, at higher frequencies such as 60 GHz, this phenomenon might have more effect on the channel. Previously, the 60 GHz measurements and analysis in the CANMET mine were carried out in different aspects such as identifying the PL exponent and delay spread values with single polarization, investigating the link reliability based on the antenna diversity gain, implementing the deterministic ray-tracing modelling using reflection and diffraction phenomenon, and the scattering analysis reported in [11–13, 33–36]. Hence we take into account different antenna polarizations in the present analysis of the underground mine wireless channel. Consequently, the polarization and scattering effects are necessary to be addressed in the underground mine channel model but are not reported in the open literature on this subject so far. Some parts of this article are archived in the first author's Ph.D. thesis reported in [35]. Some results and analysis of this article are summarized from the author's studies reported in [36–39]. In this article, the measurements and characterization are examined by considering the facts of polarization, scattering, waveguide, and antenna radiation patterns dealing with the different magnitudes of the floor, wall, and ceiling roughness in different gallery dimensions.

2 | MEASUREMENT SETUP AND EXPERIMENTAL PROTOCOL

A 60 GHz frequency domain measurement setup was used to perform the experiment in two measurement depth zones (i.e. 40 and 70 m levels) of the CANMET mine and is shown in Figure 1.

2.1 | Underground mine environment

The dimensions of the 40 m level are approximately 5 m in both height and width. From the surface roughness measurements at the 40 m gallery, the maximum, mean, and standard deviation of the roughness of the side walls were found to be around 37, 20,

TABLE 1 Example of large scale measurement results in CANMET

References	Gallery (m)	fc (GHz)	BW (GHz)	A_{tx}	A_{rx}	Tx-Rx (m)	A_{tg}	A_{rg}	n	$\overline{\tau_{rms}}$ (ns)
[3]	40	2.4	0.2	Omni	Omni	70	0	0	2.16	15–37
[6]	40	2.4	0.1	2 × 2 Omni	2 × 2 Omni	26	2.5	2.5	1.76	3.23
[7]	40	2.4	0.1	2 × 2 Patch	2 × 2 Patch	25	6–9	6–9	1.73	N/A
[8]	40	2.45	0.2	4 × 4 Patch	4 × 4 Patch	30	7	7	1.29	1.38
[9]	40	5.8	0.2	2 × 2 Patch	2 × 2 Patch	11	12	12	2.1	N/A
[10]	40	6.6	7	2 × 2 Patch	2 × 2 Patch	10	12	12	1.42	N/A
[11]	40	60.5	7	2 × 2 Patch	2 × 2 Patch	10	10	10	1.48	7.65
[12]	40	60.5	7	2 × 2 Patch	2 × 2 Patch	10	24	24	1.36	1.85
[13]	70	2.4	0.2	Omni	Omni	23	0	0	2.04	6.31
[14]	70	3.5	3	Omni	Omni	15	0	0	1.47	11.8
[15]	70	5.8	0.2	Omni	Omni	22	0	0	2.22	5.11
[13]	70	5.8	0.2	Omni	Omni	23	0	0	2.22	6.14
[16]	70	6.5	7	Horn	Horn	10	6–14	6–14	2	2.09
[16]	70	6.5	7	Omni	Horn	10	1	6–14	1.99	7.79
[16]	70	6.5	7	Omni	Omni	10	1	1	2.11	9.74
[13]	70	60	2	Horn	Horn	6	20	20	1.68	2.41

Note: n is the PL exponent; $\overline{\tau_{rms}}$ is the mean RMS delay spread; A_{tx} and A_{rx} are the transmitter (Tx) and receiver (Rx) antenna types, respectively; A_{tg} and A_{rg} are the Tx and Rx antenna gains in dBi, respectively; Tx-Rx is the approximate maximum transmitter receiver separation distance; and fc and BW are the centre frequency and bandwidth, respectively.

Abbreviation: CANMET, Canada Centre for Mineral and Energy Technology; PL, path loss; RMS, root mean square.

and 6 cm, respectively [37]. The 70 m gallery, which was narrow, had a height of around 2–2.5 m and a width of 3 m. The 70-m gallery ceiling was mostly covered with metallic nets. Some metallic pipes were present in the corner of that gallery. The floor was mostly covered with water puddles at 70 m, whereas it was drier and dustier at 40 m. The humidity in both galleries was approximately 100%. The temperature was around between 6°C and 7°C and a lower temperature was observed at 70 m compared to 40 m. There were large amounts of dust in the air at 70 m but such a large amount did not exist at 40 m gallery. A loud noise caused by the air ventilation system was also observed in both galleries. This kind of mine environment may cause a significant impact on the radio channel particularly at millimetre wavelength. Hence, the analysis of the scattering effect is described herein.

2.1.1 | Scattering effect

Scattering may create specular and diffuse reflections during the interaction between an electromagnetic (EM) wave and a rough surface which may lead to a lower or higher value of the received power at the receiver. Objects larger than the wavelength cause reflections, sharp rock edges may cause diffractions, and scattering happens when an object dimension is smaller compared to the incident wavelength. During scattering, the incident energy may distribute in coherent and incoherent ways in all angular directions.

Any object of the rough mine surface larger than 5 mm can be considered as a flat surface. Therefore, within a small scale area (i.e. 1 cm^2), an object could be larger than λ or lower than the λ or larger than λ with sharp edges. As well, the surface roughness is irregular and having higher inclinations. Moreover, the galleries consist of metallic pipes, nets, arches and water puddles. Consequently, three propagation phenomena could function randomly. Thus, a single and multiple bounced reflections, diffractions, and scattering could occur during the interaction between an EM wave and the mine surface [35]. If the scattered wave with a strong specular reflection is constructively added at the receiver, then the Rx power will increase. This phenomenon depends on the phase of the signal that could change randomly due to the diffuse scattering phenomenon.

A strong reflection in a specular direction was observed during the scattering in the galleries reported in [37]. The results show that the incident power is scattered within a range of about 10° along the specular direction of the reflected wave. Moreover, the PL difference between the reflected and the line of sight (LOS) signals is found to be around 19 dB reported in [39] where the surface material absorption and incident power dissipation may occur along with the propagation loss [40, 41]. Thus, the channel scattering and the constructive addition of the scattered paths along with the specular reflected path may increase the Rx power thereby leading to a lower value of n compared to the lower frequency bands such as 2.4 GHz.

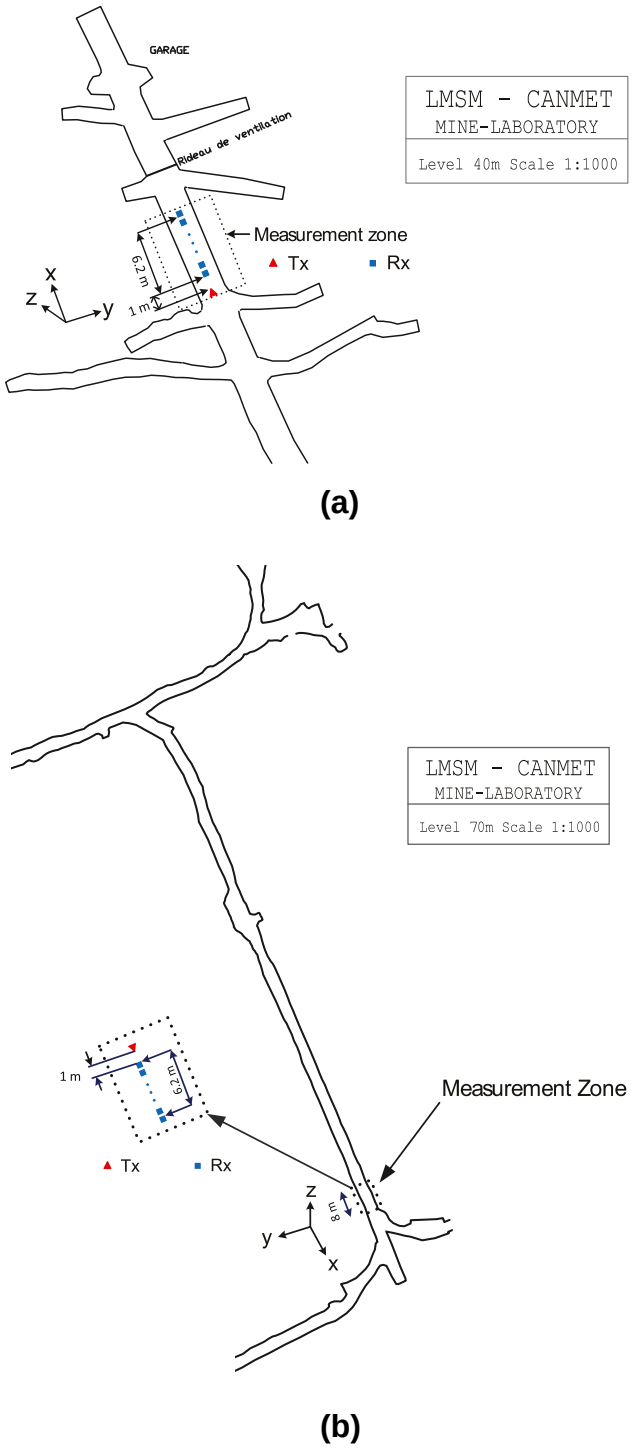

FIGURE 1 Measurement zone at (a) 40 m and (b) 70 m mine levels

2.2 | Measurement setup

The setup was designed and implemented in the CANMET underground mine in cooperation with the LRTCS laboratory. An illustration of the measurement setup is shown in Figure 2. A vector network analyzer (VNA) with a frequency band range of 40 MHz to 70 GHz was used as a two-port network measurement system for transmission and reception of the radio signal. The number of frequency points of 2000 was used for the measurement. The power amplifier was used with a gain of 30 dB. Since a high loss (almost 36.8 dB) in the 4.6 m cable was observed, even with a low noise amplifier (LNA) with 30 dB gain, the level of the signal was not strong enough to have a reflected path, therefore a second LNA was added with a gain of 18 dB to enhance the signal power. The frequency range was then selected, following the IEEE Standard 802.15.3c, between 57.24 GHz and 59.4 GHz (channel 1). Other channels in this standard were also taken into account during the measurements, but high attenuation of the radio signal was observed due to the 61 GHz upper frequency range of the QuinStar LNA. The transmit power was set at 4 dBm for the measurements. Horn and omnidirectional antennas were used to make directional and omnidirectional propagation scenarios measurements between the Tx and Rx. The Horn antenna radiation patterns were measured in the anechoic chamber as shown in Figure 3. Results showed an HPBW of about 12° in both azimuth and elevation planes. Since the horn antenna was pyramidal, the EM field radiation was mostly directive in the HH (Tx as horizontal and Rx as horizontal) polarization, whereas some strong ripples in the side lobes were observed in the VV (Tx as vertical and Rx as vertical) polarization. The vertically polarized omnidirectional antenna had an HPBW of 360° in azimuth and around 40° in the elevation direction. In order to find the polarization effect, the horizontal polarization of the omnidirectional antenna was used to observe any influence between horizontal and vertical polarizations in correlation to the communication links between the moving miners.

A similar experimental setup was used for all antenna configurations. The polarization of the antenna was changed from vertical to horizontal and vice versa, manually using a shift of 90°. A laser and a camera tripod were used in order to have an accurate placement of the Tx and Rx in LOS condition. Since the channel considered between two miners body to body link, the Tx and Rx were positioned in the middle of a gallery with a width and height of approximately 1.5 m. A list of the measurement parameters is shown in Table 2. The data acquisition was completed by connecting a computer to a VNA via a general purpose interface bus interface. A LabVIEW programme was used to control the measurement procedure and a MATLAB programme was used to move the VELMEX 3D positioning table.

2.3 | Measurement protocol

A VNA with 1 kHz intermediate frequency bandwidth (IFBW) allowed a single channel (S_{21}) full sweep time of around 6 s for 2000 points, which provided a stable state of the frequency response of the channel. The ANRITSU VNA noise floor was −107 dBm with 10 Hz of IFBW. Note that, to have the smooth operation of the measured samples within one full sweep, the IF bandwidth can be increased, as a result, the noise floor level and the measurement time will increase accordingly. Therefore, with 1000 Hz of IFBW, the VNA noise floor was −87 dBm (by increasing the IFBW to a factor-of-10 where the

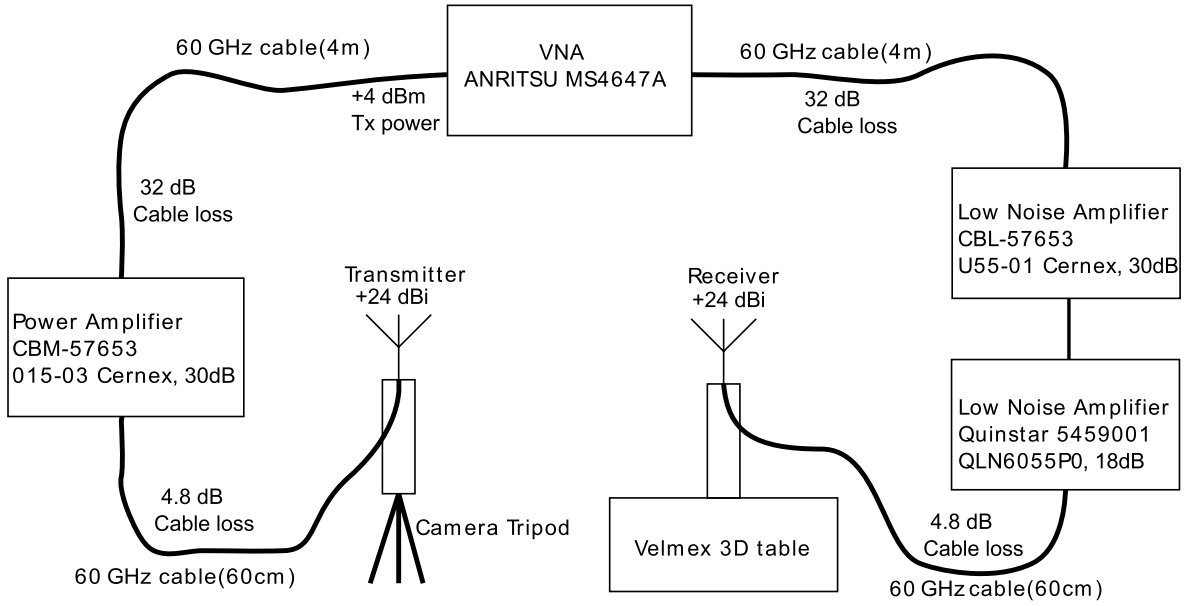

FIGURE 2 Measurement setup

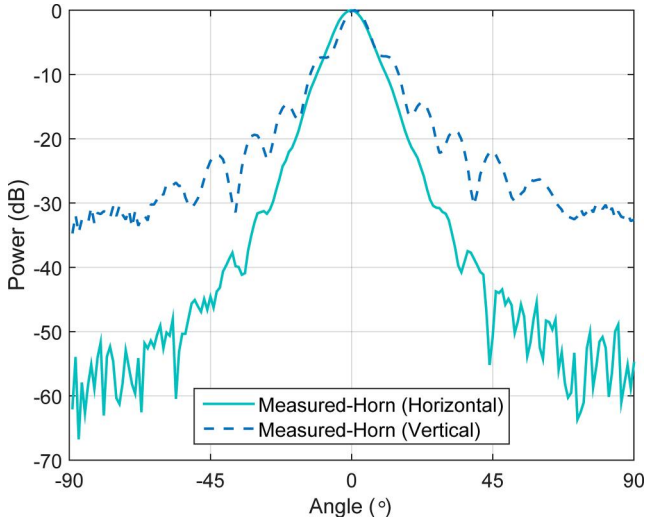

FIGURE 3 Horn antenna radiation patterns at 60 GHz

noise floor increases by 10 dB). Consequently, the dynamic range (i.e. the difference between the maximum output power and the specified noise floor) of the VNA was around 87 dB. A SOLT (short-open-load-thru) calibration with a 2.16 GHz bandwidth and 2000 sweep points spaced by 1.08 MHz was used [3].

The antenna's far-field distance (d_f) from the Tx antenna aperture was calculated using the equation as follows:

$$d_f = \frac{2D^2}{\lambda} \quad (1)$$

where D is the physical dimension (diametre) of the antenna and λ is the wavelength. The d_f of the horn and omnidirectional antennas was found to be 0.83 m and 0.58 m, respectively. Therefore, for the postprocessing of the channel impulse

TABLE 2 Summary of the 60 GHz channel measurement parameters

Mine level	40 m, 70 m
Frequency range	57.24–59.4 GHz
Bandwidth	2.16 GHz
Pyramidal horn antenna	Gain 24 dBi, HPBW 12° (Az, El)
Omnidirectional antenna	Gain 3 dBi, HPBW 360° (Az), HPBW 40° (El)
Tx and Rx height	~1.5 m
60 GHz Cable loss	7.86 dB/m

Note: Az and El are the azimuth and elevation directions, respectively.

responses, 1 m measurements were used for each configuration. Two fixed references such as a 2 m long plane of wood on the floor and a rope outside the channel were used in order to ensure the maximum accuracy of LOS. Significant time was spent to place two pieces of wood on the ground floor, which were used as rails to move the trolley (where the Velmex3D table was placed) easily. The Velmex stepping controller was able to move the Rx via a MATLAB script with a precision of 2.5 mm. For each measurement point, 15 snapshots were taken to create a local average of the channel that eliminates the effect of time varying fading.

2.3.1 | Large scale

In the large scale case, 32 measurement locations were considered with a separation of 40 λ (i.e. 20 cm), covering 1–7.2 m, as shown in Figure 4. This separation distance can be of any arbitrary value greater than λ. At each location, three consecutive measurements were taken, separated by $\lambda/2$ (2.5 mm) to have a local average of the channel which eliminates the spatial amplitude fading. Elimination of fading requires a separation distance

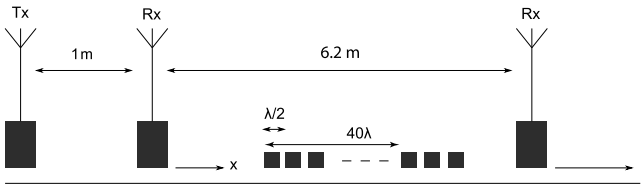

FIGURE 4 Large scale measurement procedure

of less than λ. The measurement configurations are listed in Table 3. For each configuration, 96 frequency responses were recorded for the postprocessing. The Tx position remained fixed and the Rx position moved by a distance of $\lambda/2$ and 40λ using the Velmex 3D positioning table.

2.3.2 | Small scale

In the small scale case, the study of the 3D channel characteristics was considered in order to compensate the antenna misalignment (caused by the roughness of the floor) and to eliminate the effect of spatial amplitude fading. The measurement procedure is shown in Figure 5. Two measurement locations such as at 1 m and 3 m were considered. The measurement configurations are listed in Table 4. The Velmex stepping controller was used to move the Rx in x, y, and z directions. It was observed that the floor of the galleries was inclined largely within a 1 m^2 area, particularly at 40 m. Although the LOS is aligned in the x direction, the alignments in the y and z directions were also required in order to get the maximum power between the Tx and Rx antennas. This should be noted that it was difficult to know at which point the maximum power of Rx was reached due to the rough surface. Therefore, at each distance, a $5 \times 5 \times 5$ grid points separated by a distance of $\lambda/2$ was considered for the measurement. As well, Tx and Rx were aligned at the $(\lambda, \lambda, \lambda)$ grid point and the $5 \times 5 \times 5$ grid points were recorded following a square wave trajectory (defined by the Velmex) as illustrated in Figure 5. For each antenna configuration, 250 frequency responses were recorded for the postprocessing where 125 responses were taken at each distance.

2.3.3 | Post processing

To obtain a power delay profile (PDP) of each Rx position, at first, an average of 15 snapshots of the frequency response was performed. Second, to remove the antenna effect and the cable loss, over the air calibration (i.e. a division between the 1 m complex frequency response and all complex frequency responses) was performed. Finally, an inverse fast fourier transform (IFFT) of the calibrated frequency responses was performed and the normalized PDPs were obtained. A multipath detection process was performed by the procedure described in [15]. The 1.08 MHz sweep frequency gave a temporal range of 925 ns (corresponding to the inverse of the sweep frequency), which was sufficient to observe the largest multipath excess delay (i.e. approximately 30 ns) through all sets of measurements.

TABLE 3 Large scale measurement configurations

Mine level	Antenna configuration	Polarization configuration
40 m	Horn-horn	VV, HH
40 m	Omni-horn	VV, HH
70 m	Horn-horn	VV, HH
70 m	Horn-omni	VV, HH

Abbreviations: HH, Tx as horizontal and Rx as horizontal; VV, Tx as vertical and Rx as vertical.

Figure 6 shows an example of the postprocessed normalized PDP. The strongest peak of the PDP corresponds to the first observable path. As expected, the first direct path corresponds to a delay of about 9.7 ns at 3 m Tx-Rx distance. A decrement of multipath component powers with various propagation delays is seen in Figure 6. The threshold value for the multipath detection process was set to −25 dB. The dynamic range of the measurement was around 40 dB.

3 | LARGE SCALE (i.e. <10 m) CHARACTERIZATION

Results of the large scale characterization have been analyzed by PL exponent and signal fading. The PL at a distance d is calculated by adding all incoming multipath. The free-space PL at a reference distance of 1 m (i.e., d_0) with 58.32 GHz centre frequency is set to 67.76 dB [42–44] as follows:

$$\mathrm{PL(dB)} = 67.76\ \mathrm{(dB)} + 10\log_{10}\frac{1}{K}\sum_{j=1}^{K}\sum_{i=1}^{L}|a_{ij}|^2\,\delta\{\tau-\tau_{ij}\} \quad (2)$$

where K and L are the total number of consecutive measurement points along the x direction and the total number of multipath, respectively. a_i and τ_i are the i^{th} path amplitude and delay at j^{th} location, respectively.

By computing the deviation of the PL in dB with respect to the linear regression line, the value of the signal fading was estimated. The values of the deviations were then fitted with a zero mean normal distribution to obtain the fading parameter.

The average PL for any arbitrary distance between Tx and Rx can be modelled by a lognormal (normal in dB) random distribution [42]:

$$\mathrm{PL_{dB}}(d) = \mathrm{PL_{dB}}(d_0) + 10n\log_{10}\left(\frac{d}{d_0}\right) + S_\sigma(\mathrm{dB}) \quad (3)$$

where n denotes the rate at which the received power decreases according to the Tx-Rx distance's increases. $\mathrm{PL_{dB}}(d_0)$ is the

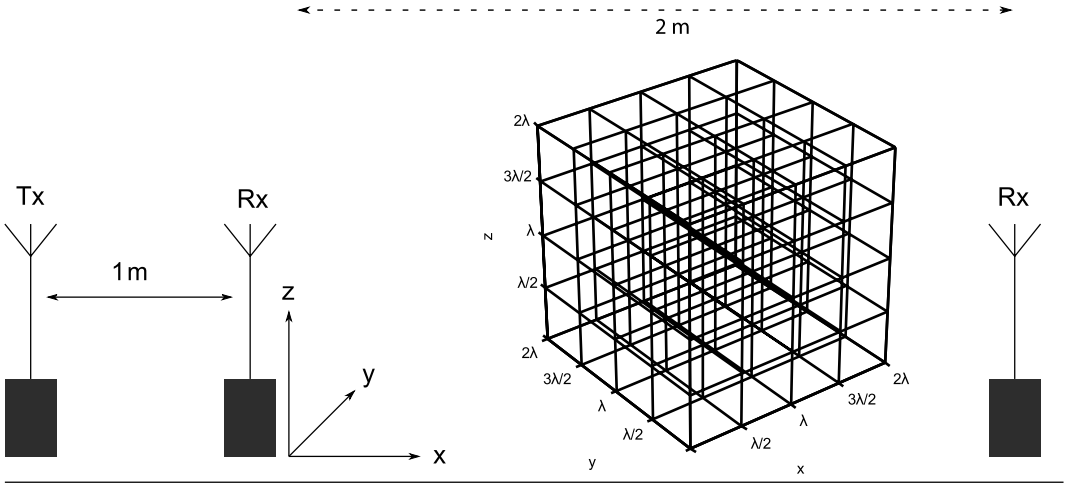

FIGURE 5 3D Small scale measurement procedure

TABLE 4 Small scale measurement configurations

Mine level	Antenna configuration	Polarization configuration
40 m	Horn-Horn	VV
70 m	Horn-Horn	VV
70 m	Horn-omni	VV

Abbreviation: VV, Tx as vertical and Rx as vertical.

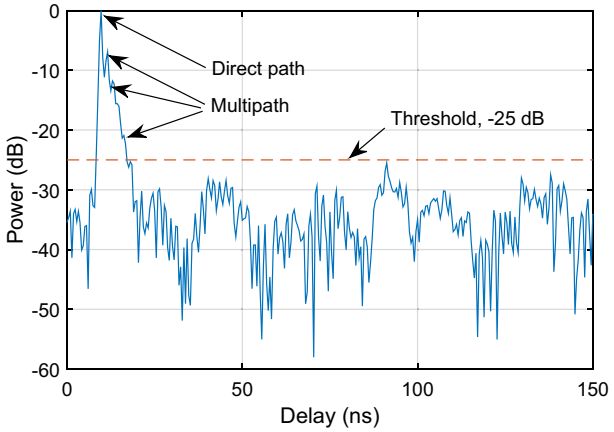

FIGURE 6 An example of a measured power delay profile of 70 m horn-horn (Tx as vertical and Rx as vertical) configuration at 3 m Tx-Rx distance

free space PL at reference distance d_0 and S_σ is a fading parameter with a zero mean Gaussian random variable in dB with a standard deviation of σ_{dB}.

3.1 | Results and discussion

3.1.1 | Path loss

An example of a scatter plot of the PL according to the Tx-Rx distance with different antenna polarizations is shown in Figure 7. The values obtained are summarized in Table 5. The linear least square regression method was used to find the value of the PL exponent n and the fading parameter σ_{dB}. The PL exponent values obtained are close to the value found in free space (i.e. $n = 2$). The results reported in [23, 45–49] also show that the PL exponents are ranging between 1.4 and 1.8 in different kinds of indoor and underground mine environments at 60 GHz. The obtained results can be explained due to the facts of scattering, polarization, antenna radiation patterns, and waveguiding effects. Those effects are explained later in section 5.

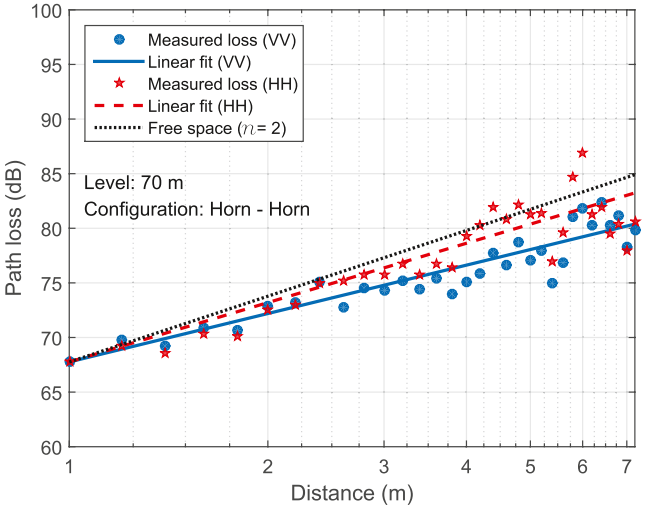

FIGURE 7 An example of a scatter plot of path loss as a function of Tx-Rx distance with horn-horn configuration at 70 m

Particularly, a differential value of n between VV and HH polarization obtained may be the cause of the different antenna radiation patterns. Due to the different roughness magnitudes of the wall, ceiling, and floor (which consist of higher inclination and sharp edges), the coherent and incoherent scattering phenomena may occur in the channel. As shown in Figure 3, the horn-horn antenna configuration may provide the

TABLE 5 Large scale measurement results

Antenna configuration	HPBW				τ_{rms}		$\bar{\tau}$		τ_{max}	
	t_x	r_x	n	dB	μ	σ	μ	σ	μ	σ
40 $m_{H-H_{VV}}$	12°	12°	1.87	1.76	1.86	0.38	0.38	0.10	28.06	7.15
40 $m_{H-H_{HH}}$	12°	12°	2.18	1.39	1.83	0.43	0.33	0.14	26.25	5.82
40 $m_{O-H_{VV}}$	360°	12°	1.10	1.12	2.66	0.56	2.06	0.69	11.51	3.58
40 $m_{O-H_{HH}}$	40°	12°	1.97	1.59	2.04	0.41	1.52	0.53	6.53	1.91
70 $m_{H-H_{VV}}$	12°	12°	1.48	1.39	1.22	0.23	0.30	0.11	10.15	3.21
70 $m_{H-H_{HH}}$	12°	12°	1.80	2.05	1.12	0.37	0.23	0.10	20.11	7.64
70 $m_{H-O_{VV}}$	12°	360°	1.11	1.53	1.40	0.59	0.60	0.30	9.89	7.47
70 $m_{H-O_{HH}}$	12°	40°	1.98	1.13	0.97	1.33	0.22	0.26	7.33	11.31

Note: τ_{rms}, $\bar{\tau}$, and τ_{max} are in nenoseconds (ns). HPBW is the half power beamwidth of antenna in azimuth plane. t_x and r_x are the transmitter and receiver, respectively.
Abbreviations: HPBW, half-power beamwidth.

diffused scattered waves, and those waves may arrive from the surface caught by the antenna side lobes with an additional value of around between 10 dB and 20 dB of power in VV polarization when compared to the HH one. With the horn and omni antenna configurations (considering the azimuth plane) a wider angle of HPBW (i.e. 360°) at the VV receiver resulting in a higher number of multipath when compared to the HH one (i.e. 40°). Therefore, the VV polarization provides more multipath components into that experimental topology, correspondingly, the constructive addition of the multipath at the receiver leads to a lower value of PL exponent compared to the HH polarization.

3.1.2 | Interference fading

Interference fading can be characterized by increasing and decreasing the signal power losses when the Rx is driven at an LOS direction in the presence of the fixed objects (e.g. rough walls, metallic pipes, nets, ventilation systems, water puddles etc.) beside a propagation path. Sharp-edged rocks that are larger than the wavelength (5 mm) can increase the effects of large scale radio signal fading due to the reflection, diffraction, and scattering, in which the signal power variations along a wireless link can be characterized by the statistical distributions. In order to quantify this, the deviations of the PL values from the linear regression line were calculated and the standard deviation of the variations (σ_{dB}) was estimated. The obtained results of σ_{dB} are summarized in Table 5. Results show that once the distance increases the value of the fading increases a bit. The value of the fading is not severe with the 60 GHz bands overall, compared to the 2.4 GHz bands, due to the use of the lower value of HPBW of antennas. An example of the cumulative distribution function (CDF) of the amplitude fading between the fitted and the measured data is plotted in Figure 8. Large scale fading in underground mines is usually found to be normally distributed [16] and was seen to all of our configurations.

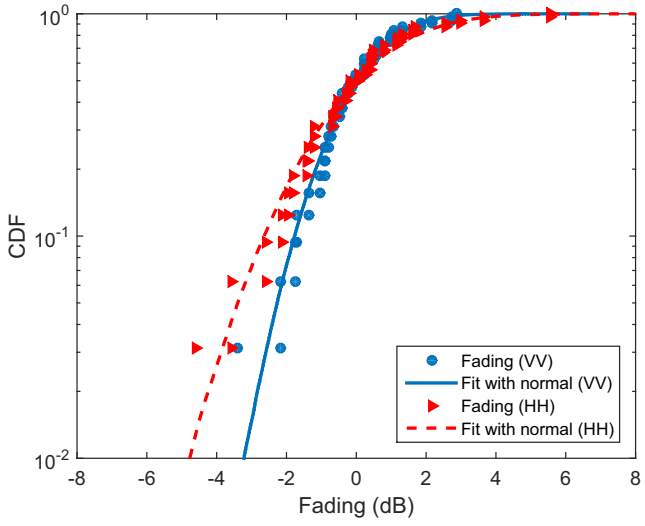

FIGURE 8 An example of the cumulative distribution functions of the fading fitted with the normal distribution at 70 m (Horn-Horn)

3.1.3 | Delay spread

The mean and standard deviation of the excess delay ($\bar{\tau}$), RMS delay spread (τ_{rms}), and the maximum excess delay (τ_{max}) of different antenna configurations from the large scale measurements (between 1 m and 7.2 m distance) were computed from the PDPs of each of the grid points followed by the Equation (5) and summarized in Table 5. Results show that the use of vertical polarization provides a higher value of τ_{rms} than the horizontal ones. Moreover, a higher value of τ_{rms} and τ_{max} is observed in a wider gallery.

Ben et al. [11] noted that the RMS delay spread is approximately 7 ns at 60 GHz in CANMET mine. Since this experiment was with MIMO channels with 60° HPBW of antennas in a different environmental topology, a higher number of multipath may arrive at the Rx with higher amplitudes and delays. On the other hand, an RMS delay spread of

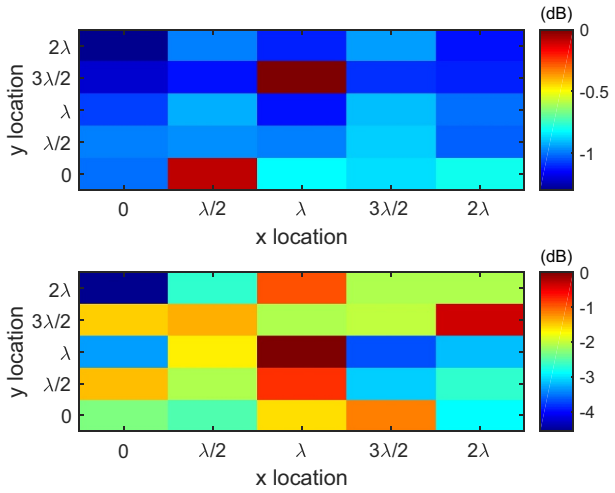

FIGURE 9 An example of the spatial distribution of multipath total power with $x \times y$ and $z = \lambda$ (which is aligned) for different antenna configurations at 70 m (the upper plot is $H - H_{VV}$ and the lower plot is $H - O_{VV}$)

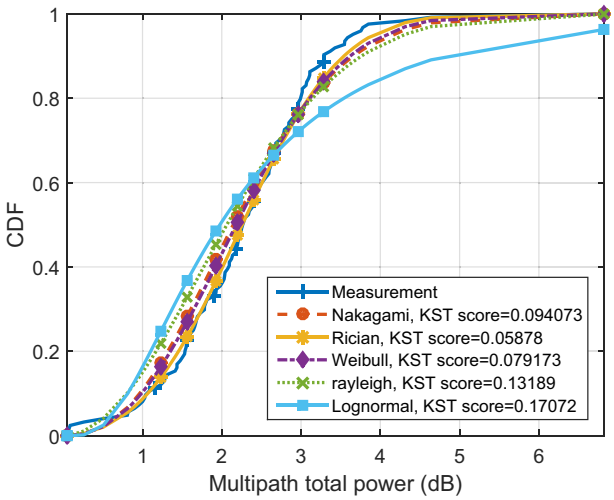

FIGURE 10 An example of small scale fading distribution with $H - O_{VV}$ configuration at 70 m

around 2 ns by using a horn antenna of 16° HPBW in the same mine is reported in [13]. The difference between the obtained results herein is due to the value of HPBW, and the experimental topology. Hence, the time dispersion results of the polarimetric measurements depend on a specific topology and antenna radiation patterns as well as the factors described later in the section 5.

4 | SMALL-SCALE (i.e. 1 cm × 1 cm × 1 cm) CHARACTERIZATION

The measured channel transfer function can also be defined as $H(f,\ t,\ d_{x,y,z})$, where $x = x_1 \ldots x_5$, $y = y_1 \ldots y_5$, $z = z_1 \ldots z_5$. Therefore, for a position $d_{x,y,z}$, the averaged measured channel impulse response can be calculated as follows:

$$h(\tau; d_{x,y,z}) = \mathrm{IFFT}\left[\frac{1}{M}\sum_{j=1}^{M} H(f, t_j, d_{x,y,z})\right] \quad (4)$$

where M is the number of snapshots taken at each time instance t, τ is the path delay, and $f = 1, 2, \ldots, 2000$. The PDP can be defined as follows [42, 50]:

$$P(\tau; d_{x,y,z}) = \sum_{i=1}^{N} |a_i(d_{x,y,z})|^2 \delta\{\tau - \tau_i(d_{x,y,z})\}, \quad (5)$$

where N is the number of multipath components, a_i and τ_i are the i^{th} path amplitude and delay, respectively. The time dispersion parameters of the channel such as the mean excess spread ($\overline{\tau}$), the maximum excess delay ($\tau_{\max}$), and the RMS delay spread (τ_{rms}) have been extracted from the PDPs followed by the Equation (5) [42, 51]. The τ_{rms} can be expressed as:

$$\tau_{\text{rms}} = E_d\{\tau_{\text{rms}}(d_{x,y,z})\}, \quad (6)$$

where $E_d\{\cdot\}$ is defined as the mean value of τ_{rms} collected from every grid points. The $\tau_{\text{rms}}(d_{x,y,z})$ at each point is mathematically defined as:

$$\tau_{\text{rms}}(d_{x,y,z}) = \sqrt{\overline{\tau^2} - (\overline{\tau})^2}, \quad (7)$$

where $\overline{\tau}$ is the mean excess delay and its first and second moments ($n = 1, 2$) expression is given below:

$$\overline{\tau^n} = \left[\sum_{i=1}^{N} a_i^2 \tau_i^n\right] / \left[\sum_{i=1}^{N} a_i^2\right], \quad n = 1, 2 \quad (8)$$

where N is the total number of paths, τ_i and a_i are the i^{th} path delay and amplitude, respectively.

4.1 | Results and discussion

4.1.1 | Fading

The normalized multipath total power (e.g. the power summation of all multipath components) of each 3D grid points was extracted from the PDPs. An example of the spatial distribution of multipath total power of 2D grid points is shown in Figure 9.

The signal power was mostly distributed throughout the grid points at 70 m compared to the 40 m gallery, caused by the narrow passage gallery. At 40 m, the power was mostly directive and a lower signal power fluctuation was observed due to the larger gallery dimension. The average small scale fading ranges were found to be from 1 to 2 dB and 3 to 5 dB for horn-horn, and horn-omni configurations, respectively. This implies that the Rx may experience around an additional

TABLE 6 3D small scale measurement results

	HPBW		τ_{rms}		$\overline{\tau}$		τ_{max}	
Antenna configuration	t_x	r_x	μ	σ	μ	σ	μ	σ
40 $m_{H-H_{VV}}$	12°	12°	1.20	0.14	0.48	0.10	22.15	0.38
70 $m_{H-H_{VV}}$	12°	12°	0.77	0.51	0.36	0.27	9.05	11.39
70 $m_{H-O_{VV}}$	12°	360°	1.62	0.71	0.89	0.45	9.07	9.62

Note: τ_{rms}, $\overline{\tau}$, and τ_{max} are in nanosecond (ns). HPBW is the half power antenna beamwidth in azimuth plane.

1–5 dB power loss when it moves by a particular cubical area (i.e. 1 cm × 1 cm × 1 cm). Therefore, the Rx displacement of $\lambda/2$ was not found to have a significant effect at 60 GHz in the mine environment.

To find the statistical characteristics of the amplitude fading, different known distributions were compared. The Kolmogorov–Smirnov test (KST) was used to identify which distribution matched best with the experimental results corresponding to the lower value of the KST score. Figure 10 shows an example of the measured CDF of multipath amplitude fading, which fits with the Rician distribution. The distribution of small scale multipath amplitudes of the LOS channel can be modelled as a Rician distribution which characterizes a stronger LOS path and scattered multipath. A comparative study of all configurations showed that Rician distribution was matched, since the Tx was directive horn antenna in the LOS direction, and a strong dominant direct path and scattered multipath arrived at the Rx [52].

4.1.2 | Delay spread

The time dispersion parameters extracted from the 3D grid points are summarized in Table 6. For H-H configuration, τ_{rms} is higher in the 40 m gallery than at 70 m gallery, because the 40 m gallery is wider and, hence, the path delays are higher. For the 70 $m_{H-O_{VV}}$ case, a higher number of multipath components is observed compared to all configurations that provide a higher value of τ_{rms}. This is due to the use of the omnidirectional antenna at the Rx, the presence of narrower gallery dimension, and metallic pipes on the channel beside the LOS direction, which may add a higher number of multipath with higher value of amplitudes at the Rx. The empirical CDF of the τ_{rms} values is illustrated in Figure 11. It seems that the standard deviation of τ_{rms} does not vary significantly and overall τ_{rms} lies between 0 ns and 4 ns.

Overall, the large- and small-scale results for both galleries show that the horn-omni and omni-horn configurations provide a higher time dispersion of the channel compared to the horn-horn configuration due to the use of the omnidirectional antenna which provides a higher fluctuation of multipath amplitudes. Around two to three multipath components were observed in horn-horn configuration versus around four to five in horn-omni or omni-horn scenarios [35]. Moreover, with a horn-horn configuration, a higher time disperse channel was observed at 70 m compared to 40 m due to the narrow gallery dimension with different magnitudes of the roughness. The directional antenna in both Tx and Rx has a major advantage to reduce the number of multipath components in the underground mine gallery and consequently maximizes the data transfer rate. Large scale and small scale results show that the signal undergoes a frequency selective fading due to the smaller value of the coherence bandwidth compared to the signal bandwidth, meaning an equalizer (adaptive tapped delay filter) will be needed at the Rx [42]. The obtained values in both galleries imply that the horn-horn antenna configuration may fulfil the mining industry requirements such as precise geolocalization and high speed connectivity due to the antenna directivity and lower signal power degradation. In addition, the use of both polarizations in the wireless system may help to enhance the system capacity. Omnidirectional antennas are not very effective at 60 GHz because of the lower directivity and gain compared to the directional antennas, but they might be appropriate for the wider signal coverage.

5 | COMPARISONS AND EFFECTS

The difference between this experiment and others performed in the CANMET underground mine is listed in Table 7. The wireless scattered channel measurements with different antenna polarizations provide an explanation to determine whether a dual or single polarization would be best suited, as well as which polarization type in underground mine. Different antenna configurations may contribute to the choice of using a directional or omnidirectional antenna in underground mine galleries. A combination of gallery depths, antenna configurations, and polarizations, as well as 3D small scale measurements, provides more channel characteristics information in terms of scattering effect compared to the other works. Consequently, some effects which caused the increment and decrement of the value of n and τ are identified. These are summarized below in order to get into depth of the scattered channel characterization.

5.1 | Waveguide effect

The waveguide effect creates a constructive addition of the multipath after having multiple bounced reflections in a tunnel, corridor which phenomenon leads to a higher value of the received power at the receiver. The waveguide effect defines where a direct path and a slightly delayed path (or paths) from the surface are combined at the receiver in such a way where the waves are being guided along a particular direction. Generally, this effect occurred at a larger Tx-Rx distance where the reflects waves can travel along the propagation direction after having multiple bounces from the surrounding surface.

This effect is seen in CANMET underground mine galleries at larger Tx-Rx distance (i.e. >10 m) and at lower frequency bands (i.e. 2.4 GHz) [3, 6–8]. Results of the angular dispersion measurements in CANMET at 60 GHz also show

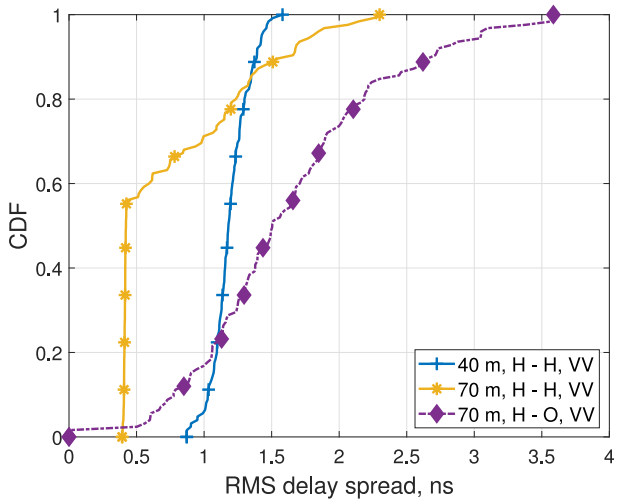

FIGURE 11 Cumulative distribution function of root mean square delay spread values

TABLE 7 Difference with other CANMET 60 GHz experiments

Reference	Gallery	Pols	Ants	n	$\overline{\tau^l_{rms}}$	2D $\overline{\tau^s_{rms}}$	3D $\overline{\tau^s_{rms}}$
[11]	40 m	×	×	✓	✓	×	×
[12]	70 m	×	×	✓	✓	✓	×
[13]	70 m	×	×	✓	✓	×	×
This work	40 m, 70 m	✓	✓	✓	✓	×	✓

Note: Pols and Ants refer to the measurement results obtained with different antenna polarizations (i.e. V and H) and different antenna configurations (i.e. horn-horn, horn-omni etc.), respectively. n, τ^l_{rms}, and τ^s_{rms} denote the path loss exponent, the large scale, and the small scale RMS delay spreads, respectively.

that the angular spreads of multipath are proportional to the gallery dimensions and inversely proportional to the Tx-Rx distances [36]. The results revealed that no reflected paths were received at the receiver after around 4 m. Therefore, this waveguide effect might not be the only explanation for the results obtained herein at a 10 m Tx-Rx distance. At this short distance, the specular reflections may travel until one or two bounces. Since the surface is highly rough, the 5 mm wavelength may additionally create multiple bounces of reflections due to the scattering phenomenon. Consequently, the received power may increase due to the constructive addition of the scattered multipath which leads to having a lower value of n compared to the free space. The results also show that the waveguide phenomenon is more in pronounced in the narrower gallery which also implies a lower value of n compared to the wider one.

5.2 | Polarization effect

The polarization effect may introduce a differential value between V and H polarized antenna received power. Further, a single polarized wave may change its polarization states during the interaction with the rough surface.

The horizontal and vertical polarization orientations of an antenna can be used to measure the Fresnel reflection coefficient parameters denoted as $|\Gamma_\perp|$ and $|\Gamma_\parallel|$, respectively [39, 53]. The results show that the values of the reflection coefficients of limestone, glass, and brick materials are different at 1.9 and 4 GHz [54]. Therefore, the value of the reflection coefficients depends on the electric field orientations, the plane of the incident, operating frequency, and dielectric properties of the materials.

At 60 GHz, results show that the value of reflection coefficient varies severely as the incident angle varies [53]. As well, the AoAs of the reflected waves depend on the value of reflection coefficients as reported in [26]. Results reported in [27, 29] also show that the polarization types have a significant impact on the 60 GHz channel. This kind of inhomogeneous, irregular rough surface of the galleries may consist of materials such as rocks, sand, minerals etc. where those can be reflective and dispersive at 60 GHz. Therefore, the V and H polarized antennas with different values of roughness of the floor, wall, and ceiling may provide a differential value of $|\Gamma_\perp|$ and $|\Gamma_\parallel|$.

In addition, the incident wave could change the polarization types during the interaction between the EM wave and the rough surface. Consequently, the new polarized signal may not receive at the single previously polarized antenna state at the receiver. This phenomenon may provide a lower value of the multipath total power which may lead to have a lower value of τ. However, the cross-polarization experiment could provide a more in-depth analysis of this effect in the future.

5.3 | Antenna beam pattern effect

Different antenna beam patterns may increase and decrease the number of multipath at the receiver due to the antenna HPBMs and side lobes. The vertical configuration of the horn antenna beam pattern has strong ripples (i.e. around 20 dB compared to the horizontal) in the side lobes between ±20° and ±60° as shown in Figure 3. This kind of beam pattern may provide a higher value of the multipath total power at the receiver. Consequently, a constructive addition of the multipath provides a higher value of τ which in turn leads to having a lower value of n compared to the horizontal configuration. This effect is also observed in other measurements as reported in Table 1 which shows that a higher value of HPBW causes a higher number of multipaths at the receiver which also leads to a higher value of the delay spread.

6 | CONCLUSIONS

The results and analysis of the 60 GHz channel measurements for underground mine applications are presented in this work. The channel characteristics with different polarizations and different types of antennas in different gallery depths are highlighted. The comparative study of the large scale (i.e.

<10 m) results show that the PL exponent is close to one of the free-spaces because of the constructive combination of the multipath components at the Rx where the channel is impacted by the scattering, polarization, antenna beam pattern, and waveguide effects. The results also show that the RMS delay spread lies between 0 and 4 ns. A 3D small scale (i.e. 1 cm × 1 cm × 1 cm) measurement has been carried out for compensating the antenna misalignment issues where the amplitude fading lies between 1 dB and 5 dB within a small scale area. The channel presents less time dispersion in wider gallery compared to the narrower one. The Rician distribution provides a better fit with the results of the small scale multipath total power.

The use of vertical polarization on directional and omni-directional antennas has provided a higher number of multi-paths at the Rx implying a higher value of the delay spread when compared to the horizontal one in this particular experimental topology. The irregular rough surface, which generates scattering, has a direct impact on the amplitude, phase, and delay of the channel severely compared to the lower frequency bands. In addition, polarization, antenna beam pattern, and waveguide effects may create a significant change in the channel characteristics at 60 GHz bands. In order to deal with the scattering, the system designer may define a lower antenna beam resolution to have a highly directive propagation links. To compensate with the polarization effect, the use of dual polarization at the antenna would be a good choice. Therefore, by taking into account the beamforming feature deployment in the point to point communication links, a directive narrow beam less than 10° HPBW with dual-polarization of the antenna could be the good choice for the wireless system design in this particular environment at 60 GHz. These results can be used to understand the amplitude and time dispersion, and the effects such as scattering, polarization, and antenna beam pattern of the scattered channel which can support the design and development of a high-speed wireless system in this particular underground environment.

ACKNOWLEDGEMENT

This work was supported by the Natural Sciences and Engineering Research Council of Canada (NSERC), Bell Alliant, Newtrax Capital Regional District (CRD) Project, and NSERC Collaborative Research and Training Experience (CREATE) Pervasive and Smart Wireless Applications for the Digital Economy (PERSWADE) Programme. Special thanks to Dr. Mohamad El Khaled, Birahima Ndiaye to help during the underground measurement campaigns at Val-d'Or, QC, Canada. Thanks for the valuable guidance and support of Prof. Mourad Nedil, Prof. Nahi Kandil, Prof. Nadir Hakem, Mr. Mohamed Ailas, Dr. Yacouba Coulibaly, and colleagues at Poly-Grames Research Center and at Laboratoire deRecherche Télébec en Communications Souterraines (LRTCS).

ORCID

Sofiène Affes https://orcid.org/0000-0002-1729-3503

REFERENCES

1. Yong, S.K., Xia, P., Garcia, A.V.: 60 GHz Technology for Gbps WLAN and WPAN: From Theory to Practice. Wiley (2011). https://onlinelibrary.wiley.com/doi/book/10.1002/9780470972946
2. Murphy, R.R., et al.: Mobile robots in mine rescue and recovery. IEEE Robot. Autom, Mag. 16(2), 91–103 (2009)
3. Nerguizian, C., et al.: Radio-channel characterization of an underground mine at 2.4 GHz. IEEE Trans. Wireless Commun. 4(5), 2441–2453 (2005)
4. Canadian mining journal. http://www.canadianminingjournal.com/features/rajant-tackles-minings-big-communications-challenges. Accessed 20 December 2020
5. Mining magazine. https://www.miningmagazine.com/fleet/news/1397049/zte-trials-5g-autonomous-trucks-at-chinese-mine. Accessed 20 December 2020
6. Coulibaly, Y., et al.: Experimental characterization of a MIMO underground mine channel at 2.45 GHz. Prog. Electromagn. Res. B. 50, 219–234 (2013)
7. Ben, I., et al.: Experimental characterization of a wireless MIMO channel at 2.4 GHz in underground mine gallery. Prog. Electromagn. Res. Lett. 29, 97–106 (2012)
8. Ghaddar, M., et al.: Multiple-input multiple-output beam-space for high-speed wireless communication in underground mine. IET Microw. Antennas Propag. 10(1), 8–15 (2016)
9. Mnasri, B., et al.: Experimental characterization of wireless MIMO channel at 5.8 GHz in underground gold mine. Prog. Electromagn. Res. C. 36, 169–180 (2013)
10. Mabrouk, I.B., et al.: Line of sight MIMO-UWB short range communication in underground mine tunnel. In: 9th European Conference on Antennas and Propagation (EuCAP), Lisbon, pp. 1–4 (2015)
11. Ben, I., et al.: Feasibility of a millimeter wave MIMO system for short range wireless communications in an underground gold mine. IEEE Trans. Antennas Propag. 61(8), 4296–4305 (2013)
12. Ghaddar, M., et al.: Mm-waves propagation measurements in underground mine using directional MIMO antennas. IET Microw. Antennas Propag. 10(5), 517–524 (2016)
13. Hakem, N., Delisle, G., Coulibaly, Y.: Radio-wave propagation into an underground mine environment at 2.4 GHz, 5.8 GHz and 60 GHz. In: 8th European Conference on Antennas and Propagation (EuCAP), The Hague, pp. 3592–3595 (2014) https://doi.org/10.1109/EuCAP.2014.6902607
14. Chehri, A., Fortier, P., Tardif, P.M.: CTHp1-8: measurements and modeling of line-of-sight UWB channel in underground mines. In: IEEE Global Telecommunications Conference (GLOBECOM), Francisco, pp. 1–5 (2006)
15. Boutin, M., et al.: Radio wave characterization and modeling in underground mine tunnels. IEEE Trans. Antennas Propag. 56(2), 540–549 (2008)
16. Rissafi, Y., Talbi, L., Ghaddar, M.: Experimental characterization of an UWB propagation channel in underground mines. IEEE Trans. Antennas Propag. 60(1), 240–246 (2012)
17. Coulibaly, Y., et al.: Experimental characterization of the UWB channel for an underground mining vehicle. In: 7th European Conference on Antennas and Propagation, Gothenburg, pp. 2331–2334. EuCAP (2013)
18. Forooshani, A.E., et al.: A survey of wireless communications and propagation modeling in underground mines. IEEE Commun. Surv. Tutor. 15(4), 1524–1545 (2013)
19. Emslie, A., Lagace, R., Strong, P.: Theory of the propagation of UHF radio waves in coal mine tunnels. IEEE Trans. Antennas Propag. 23(2), 192–205 (1975)
20. Zhang, Y.P., Hwang, Y., Kouyoumjian, R.G.: Ray-optical prediction of radio-wave propagation characteristics in tunnel environments. IEEE Trans. Antennas Propag. 46(9), 1337–1345 (1998)
21. Lienard, M., Degauque, P.: Natural wave propagation in mine environments. IEEE Trans. Antennas Propag. 48(9), 1326–1339 (2000)
22. Smulders, P: Exploiting the 60 GHz band for local wireless multimedia access: prospects and future directions. IEEE Commun. Mag. 40(1), 140–7 (2002)

23. Smulders, P.F.M.: Statistical characterization of 60 GHz indoor radio channels. IEEE Trans. Antennas Propag. 57(10), 2820–2829 PART 1 (2009)
24. Geng, S., Kivinen, J., Vainikainen, P.: Propagation characterization of wideband indoor radio channels at 60 GHz. In: IEEE International Symposium on Microwave, Antenna, Propagation and EMC Technologies for Wireless Communications, Beijing, pp. 314–317. (2005). https://doi.org/10.1109/MAPE.2005.1617912
25. Yildirim, F., Sadri, A.S., Liu, H.: Polarization effects for indoor wireless communications at 60 GHz. IEEE Commun. Lett. 12(9), 660–662 (2008)
26. Sawada, H., et al.: Polarization dependence in double directional propagation channel at 60 GHz. In: IEEE International Symposium on Personal, Indoor and Mobile Radio Communications (PIMRC), Tokyo, pp. 3010–3014. (2009). https://doi.org/10.1109/PIMRC.2009.5450006
27. Manabe, T., et al.: Polarization dependence of multipath propagation and high-speed transmission characteristics of indoor millimeter-wave channel at 60 GHz. IEEE Trans. Veh. Technol. 44(2), 268–274 (1995)
28. Zhao, X., et al.: Polarization behaviours at 2.5 and 60 GHz for indoor mobile communications. Springer - An Int. J. Wirel. Pers. Commun. 27(2), 99–115 (2003)
29. Maltsev, A. et al.: Statistical channel model for 60 GHz WLAN systems in conference room environment. In: Proceedings of the Fourth European Conference on Antennas and Propagation, Barcelona, pp. 1–5 (2010)
30. Cawley, J.C.: An Assessment of Leaky Feeder Radio Systems in Underground Mines, pp. 25-1–25-15.US Department of the Interior Bureau of Mines (1989). https://www.cdc.gov/niosh/mining/userfiles/works/pdfs/aaolf.pdf
31. Zhang, Y.P., Zheng, G.X., Sheng, J.H.: Radio propagation at 900 MHz in underground coal mines. IEEE Trans. Antennas Propag. 49(5), 757–762 (2001)
32. Bashir, S.: Effect of antenna position and polarization on UWB propagation channel in underground mines and tunnels. IEEE Trans. Antennas Propag. 62(9), 4771–4779 (2014)
33. Ait Taleb, H., et al.: On 60 GHz MIMO diversity in an underground mine propagation channel. IEEE Antennas Wirel. Propag. Lett. 19(10), 1769–1773 (2020)
34. Ghaddar, M., et al.: Deterministic modeling of 5G millimeter-wave communication in an underground mine tunnel. IEEE Access. 7, 116519–116528 (2019)
35. Tariq, S.A.M.: Characterization and modelling of scattered wireless channel at 60 GHz in an underground mine gallery. PhD thesis. Electrical Engineering Department, Universitéde Montréal-École Polytechnique (2016). https://publications.polymtl.ca/2289/1/2016_ShahAhsanuzzamanMdTariq.pdf
36. Tariq, S.A.M., et al.: Angular dispersion of a scattered underground wireless channel at 60 GHz. IEEE Access. 8, 67572–67580 (2020)
37. Tariq, S.A.M., et al.: Rough surface scattering analysis at 60 GHz in an underground mine gallery. In: IEEE International Conference on Communications Workshops (ICC), Sydney, pp. 724–729 (2014). https://doi.org/10.1109/ICCW.2014.6881285
38. Tariq, S.A.M., et al.: Experimental results of Rician K-factor and co-polarization ratio of 60 GHz wireless channel in an underground mine gallery. In: IEEE International Conference on Ubiquitous Wireless Broadband (ICUWB), Montreal, pp. 1–5 (2015). https://doi.org/10.1109/ICUWB.2015.7324451
39. Tariq, S.A.M., et al.: Scattering effect based on measurements of reflection coefficients at 60 GHz in an underground mine gallery. In: IEEE 25th Annual International Symposium on Personal, Indoor, and Mobile Radio Communication (PIMRC), Washington, pp. 217–221 (2014). https://doi.org/10.1109/PIMRC.2014.7136163
40. Violette, E.J., et al.: Millimeter-wave propagation at street level in an urban environment. IEEE Trans. Geosci. Remote Sens. 26(3), 368–380 (1988)
41. Maltsev, A., et al.: Experimental investigations of 60 GHz WLAN systems in office environment. IEEE J. Sel. Areas Commun. 27(8), 1488–1499 (2009)
42. Rappaport, T.S.: Wireless Communications: Principles and Practice. Prentice Hall PTR (2002). https://www.pearson.com/us/higher-education/program/Rappaport-Wireless-Communications-Principles-and-Practice-2nd-Edition/PGM91547.html
43. Samimi, M., et al.: 28 GHz Angle of arrival and angle of departure analysis for outdoor cellular communications using steerable beam antennas in New York city. In: IEEE 77th Vehicular Technology Conference, pp. 1–6. VTC Spring, Dresden (2013). https://doi.org/10.1109/VTCSpring.2013.6691812
44. Saleh, A.A.M., Valenzuela, R.: A statistical model for indoor multipath propagation. IEEE J. Sel. Areas Commun. 5(2), 128–137 (1987)
45. Lounis, C., et al.: Large scale characterization of an underground mining environment for the 60 GHz frequency band. In: International Conference on Wireless Communications in Unusual and Confined Areas, pp. 1–4. ICWCUCA Clermont-Ferrand, (2012). https://doi.org/10.1109/ICWCUCA.2012.6402506
46. Geng, S., et al.: Millimeter-wave propagation channel characterization for short-range wireless communications. IEEE Trans. Veh. Technol. 58(1), 3–13 (2009)
47. Piersanti, S., Annoni, L.A., Cassioli, D.: Millimeter waves channel measurements and path loss models. In: IEEE international conference on communications, Ottawa, 4552–4556. (2012). https://doi.org/10.1109/ICC.2012.6363950
48. Moraitis, N., Constantinou, P.: Indoor channel measurements and characterization at 60 GHz for wireless local area network applications. IEEE Trans. Antennas Propag. 52(12), 3180–3189 (2004)
49. Zwick, T., Beukema, T.J., Nam, H.: Wideband channel sounder with measurements and model for the 60 GHz indoor radio channel. IEEE Trans. Veh. Technol. 54(4), 1266–1277 (2005)
50. Yang, H., Smulders, P.F.M., Herben, M.H.A.J.: Channel characteristics and transmission performance for various channel configurations at 60 GHz. EURASIP J. Wirel. Commun. Netw. 2007(1), 43–43 (2007)
51. Moraitis, N., Constantinou, P.: Measurements and characterization of wideband indoor radio channel at 60 GHz. IEEE Trans. Wirel. Commun. 5(4), 880–889 (2006)
52. Schothier, J.: WP3-Study: the 60 GHz Channel and Its Modelling IST-2001-32686 Broadway, 32686 (2003). https://scholar.googleusercontent.com/scholar.bib?q=info:dLsfsGw1YGEJ:scholar.google.com/&output=citation&scisdr=CgUjoxTPELD3i5k2i-U:AAGBfm0AAAAAYGEzk-WA5KP9-qtsWyney4pMoiBiz_Zb&scisig=AAGBfm0AAAAAYGEzk_K_DLv4SGUeLd7I4tCUDsNevnKl&scisf=4&ct=citation&cd=-1&hl=en
53. Ahmadi-Shokouh, J., et al.: Reflection coefficient measurement for house flooring materials at 57-64 GHz. In: IEEE Global Telecommunications Conference (GLOBECOM), Honolulu, pp. 1–6. (2009). https://doi.org/10.1109/GLOCOM.2009.5425497
54. Landron, O., Feuerstein, M.J., Rappaport, T.S.: A comparison of theoretical and empirical reflection coefficients for typical exterior wall surfaces in a mobile radio environment. IEEE Trans. Antennas Propag. 44(3), 341–351 (1996)

How to cite this article: Tariq SAM, Despins CL, Affes S, Nerguizian C. Characterization of a 60 GHz scattered wireless channel with different antenna polarizations for underground multimedia applications. *IET Microw. Antennas Propag.* 2021;15:1063–1075. https://doi.org/10.1049/mia2.12116